Ru/NiMnB spherical cluster pillar for highly proficient green hydrogen electrocatalyst at high current density

Md Ahasan Habib, Shusen Lin, Mehedi Hasan Joni, Sumiya Akter Dristy, Rutuja Mandavkar, Jae-Hun Jeong *, Jihoon Lee *

Department of Electronic Engineering, College of Electronics and Information, Kwangwoon University, Nowon-gu, Seoul 01897, Republic of Korea

A B S T R A C T

Advanced OER/HER electrocatalytic alternatives are crucial for the wide adaptation of green hydrogen energy. Herein, Ru/NiMnB spherical cluster pillar (SCP), denoted as Ru/NiMnB, is synthesized using a combination of electro-deposition and hydrothermal reaction. Systematic investigation of Ru doping in the NiMnB matrix revealed significant improvements in electrocatalytic performance. The Ru/NiMnB SCPs demonstrate superior OER/HER activity with low overpotentials of 150 and 103 mV at 50 mA/cm^2 in 1 M KOH, making them highly competitive with state-of-the-art electrocatalysts. Remarkably, the Ru/NiMnB SCPs exhibit a low 2-E cell voltage of 2.80 V at ultra-high current density of 2,000 mA/cm^2 in 1 M KOH, outperforming the standard benchmark electrodes of RuO$_2$ || Pt/C, thereby positioning Ru/NiMnB as one of the best bifunctional electrocatalysts. These SCPs exhibit exceptional high-current characteristics, stability and corrosion resistance, as evidenced by continuous operation at 1,000 mA/cm^2 high-current density for over 150 h in 6 M KOH at elevated temperatures under harsh industrial conditions. Only a small amount of Ru incorporation significantly enhances the electrocatalytic performances of NiMnB, attributed to increased active sites and improved intrinsic properties such as conductivity, adsorption/desorption capability and reaction rates. Consequently, Ru/NiMnB SCPs present a promising bi-functional electrode concept for efficient green H$_2$ production.

© 2024 Science Press and Dalian Institute of Chemical Physics, Chinese Academy of Sciences. Published by ELSEVIER B.V. and Science Press. All rights are reserved, including those for text and data mining, AI training, and similar technologies.

1. Introduction

Exploring climate-friendly and renewable energy alternatives has become essential in the context of ever-increasing demands and serious environmental challenges posed by the massive usage of fossil fuels [1]. Hydrogen is considered one of the most promising energy resources due to its high gravimetric energy density of ~142 Mj kg^{-1}, zero carbon emission and recyclability, etc. [2,3]. Among the various methods for hydrogen production, electrochemical water splitting is the only approach to generate ultrapure green hydrogen [4]. This process consists of two half-cell reactions: the anodic oxygen evolution reaction (OER) and the cathodic hydrogen evolution reaction (HER) [5]. While, the Pt/C and RuO$_2$/IrO$_2$ are the benchmark electrocatalysts for HER and OER, respectively, their limited natural reserves and high cost

hinder wide adoption [6,7]. Therefore, developing cost-effective OER/HER electrocatalytic alternatives with superior performance and stability is urgent. The catalytic operation in high alkaline concentration at large-current density and industrial temperature is necessary for advanced electrocatalysts.

In recent decades, transition metals (TMs) with the d-orbital electrons, i.e., Co, Ni, Fe, Mn, W, have been widely studied with the combination with non-metallic compounds such as phosphides, sulfides, nitrides, carbides, etc. to create cost-effective alternative electrodes [8,9]. Each metallic element's electrocatalytic advantages can be harnessed through the combination of multiple TMs. For example, nickel (Ni) is known for its excellent OER properties, while manganese (Mn) enhances HER performance. Ni is abundant and demonstrates superior water splitting (WS) capabilities due to its high reaction intermediate absorption properties [10]. Mn, with its multiple valence states (+2 to +7), exhibits favorable WS characteristics, such as high electron transfer capacity [11]. For example, Ni-B-P microspheres demonstrated exceptional OER capabilities, benefitting from low charge transfer

resistance, high surface area and fast H_2O decomposition rate [12]. Similarly, CoMnB has shown superior HER performance with high electrochemical surface area [13]. In terms of the non-metallic element, boron (B) is attracting attention due to its multi-bonding orbital characteristics and tunable charge transfer capability [14]. More recently, it has shown exceptional stability with robust multi-bonding characteristics [15]. For example, the W_3CoB_3 exhibited improved HER/OER activities, low overpotential and high reaction kinetics with its strong elemental interactions [16]. Additionally, heteroatom doping within existing TM compound matrices can directly improve catalytic properties and performance [17]. This approach, which involves inserting heteroatoms, increases active sites, enhances intrinsic activity and improves structural stability [18]. Doping is also cost-effective, requiring only a small amount of material, typically a few percent of the full electrode [18]. Ruthenium (Ru) is a desirable dopant due to its suitable adsorption/dissociation energy for water splitting reaction intermediates and relatively low cost (only 5% of Pt) [19]. Ru-based electrocatalysts can facilitate both HER and OER, making Ru doping on NiMnB a promising approach to constructing advanced electrocatalysts. However, this has not yet been attempted.

In this work, Ru-doped NiMnB spherical cluster pillars (SCPs), namely Ru/NiMnB SCPs, are successfully fabricated for the first time as illustrated in Fig. S1. Initially, NiMnB cluster pillars are synthesized via electrodeposition, followed by Ru atom incorporation through hydrothermal reaction and post-annealing. The Ru doping parameters such as doping duration, doping temperature and dopant concentration, etc. are thoroughly investigated to optimize electrocatalytic properties. The Ru/NiMnB SCPs exhibit superior OER/HER performance, comparable to the HER benchmark Pt/C and surpassing the OER benchmark RuO_2. These SCPs also demonstrate excellent bi-functional characteristics, evidenced by a low cell voltage of 2.80 V at 2,000 mA/cm^2 in 1 M KOH. Furthermore, it exhibits exceptional high-current characteristics, superior stability and anti-corrosion resistance under industrial high temperatures and alkaline solutions. This work offers valuable insights into constructing efficient and stable electrocatalytic alternatives for green hydrogen generation.

2. Material and methods

2.1. Synthesis of NiMnB electrocatalyst

In this work, Ru-doped NiMnB (Ru/NiMnB) spherical cluster pillar (SCP) electrocatalyst was newly developed by the combination of electrochemical deposition and hydrothermal reaction as illustrated in Fig. S1. The 3-D porous Ni foam (NF) was adapted as a substrate (size 1×1 cm^2) for NiMnB preparation. The 0.075 M $NiCl_2 \cdot 6H_2O$ for Ni, 0.075 M $MnSO_4 \cdot H_2O$ for Mn, 0.5 M H_3BO_3 for B, 2 M NH_4Cl and 1 M NaCl were used as precursors and dissolved in 30 mL DI water under magnetic stirring. The NH_4Cl and NaCl were utilized as electro-crystallization and pH-balancing agents for strong intermolecular interaction and nucleation [13,20]. First, the NiMnB SCP template was fabricated on NF by electrodeposition at 2 A/cm^2 for 300 sec in three-electrode (3-E) electrochemical analyzer (Wizmac, Republic of Korea) as shown in Fig. S1(a-1). The NF, graphite and Ag/AgCl were adapted as working, counter and reference electrodes for the electrodeposition growth of NiMnB. Each synthesis parameter such as molar concentration, operational current, electrochemical duration, temperature, etc. were systematically optimized. The NiMnB/NF was removed from the deposition solution and cleaned with DI water before drying in the air.

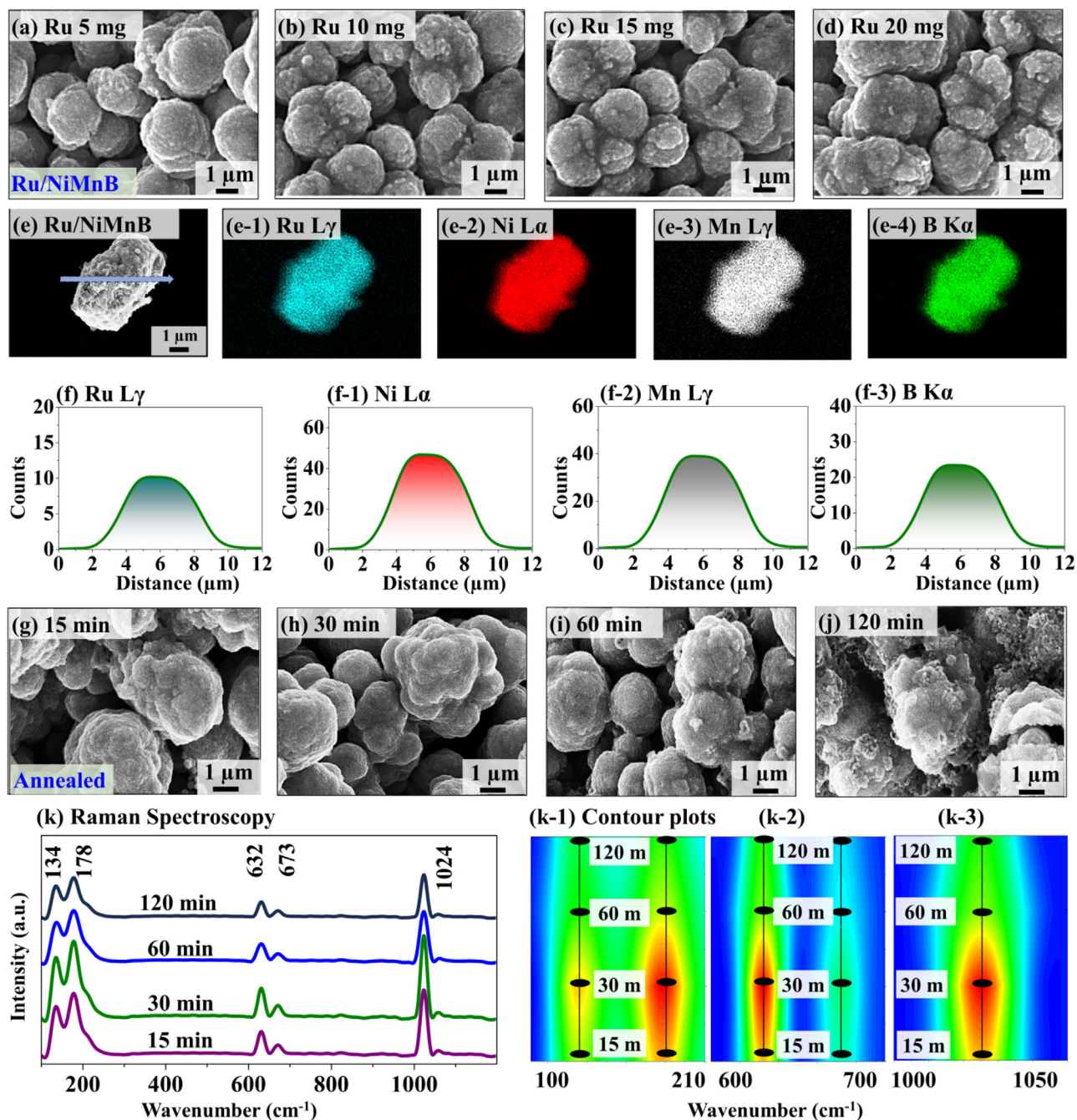### 2.2. Synthesis of Ru/NiMnB electrocatalyst

Once NiMnB was ready, the Ru doping was performed through a hydrothermal reaction as illustrated in Fig. S1(a-2). The Ru dopant (as $RuCl_3 \cdot xH_2O$) was dissolved in 30 mL of DI water. The prepared solution was transferred to hydrothermal reactor with NiMnB/NF template. Then, the reactor was placed in an oven for Ru-doping hydrothermal deposition. Various Ru doping parameters such as molar concentration, doping duration and doping temperature were systematically evaluated on NiMnB to obtain effective Ru doping conditions in the hydrothermal reaction as illustrated in Figs. S10–S20. In addition, the hydrothermal co-deposition approach was evaluated for Ru doping as seen in Figs. S21–S24, but it resulted in lower performances as compared to the separate hydrothermal doping and specific details can be found in the related section. After cooling the reaction to room temperature, the Ru/NiMnB was obtained. The optimal hydrothermal doping parameters were determined to be 15 mg Ru at 100 °C and 4 h of reaction on NiMnB template. Finally, the Ru/NiMnB was treated with optimized post-annealing (at 100 °C for 30 min) in a rapid thermal processing (RTP) system to improve overall crystallinity and electrochemical properties as illustrated in Fig. S1(a-3).

The detailed synthesis of Ru/NiMnB SCPs, experimental materials and method descriptions can be found in the supplementary texts S-1.1–S-1.5.

3. Result and discussion

3.1. Morphology and structural characterizations

The morphologies of Ru/NiMnB electrodes with Ru doping concentration variations are shown in Fig. 1(a)–(d). In this work, NiMnB is used as a cost-effective catalytic substrate mainly due to its multi-component synergistic effect, structural and electrochemical advantages. For example, Ni possesses higher intrinsic OER properties due to suitable interaction with reactants, electrical conductivity and highly electroactive oxidation states (NiOOH) [21]. On the other hand, Mn can offer prominent catalytic properties with multi-valance states, accelerating OWS capabilities [22]. B can create strong bonding with metallic elements and thus can offer superior structural stability with lower overpotentials [16]. The Ru molar concentration was controlled on NiMnB between 5 and 20 mg at 100 °C for 12 h of hydrothermal reaction. The Ru/NiMnB SCPs did not show any visible morphological differences along with Ru molar concentration variations. The spherical cluster morphology of Ru/NiMnB can demonstrate promising OER/HER characteristics. The appropriate Ru molar concentration can play a key role in determining the OWS performance by altering the adsorption capacities of H$^+$ & OH$^-$ intermediates [23,24]. The EDS top-view maps revealed Ru Lγ, Ni Lα, Mn Lγ and B Kα phases as seen in Fig. 1(e)–(e-4), suggesting successful Ru incorporation. Further, the EDS line scan profile confirmed the uniform distribution of elements as seen in Fig. 1(f)–(f-3). The best Ru/NiMnB SCPs were treated between 15 and 120 min at 100 °C fixed temperature as presented in Fig. 1(g)–(j). The samples showed similar SCP morphologies up to 60-min annealing, then visible structural deformation was observed at 120 min likely due to the excessive thermal mass. Initially, the Ru/NiMnB SCPs crystal lattice may contain various internal defects and atom dislocations due to the forced incorporation of Ru atoms under hydrothermally synthesized conditions [25]. The post-annealing was adapted on Ru/NiMnB to improve the overall crystallinity by optimizing various lattice defects/dislocations. Effective annealing treatment can improve the crystal quality by minimizing lattice defects with atomic diffusion [16,26]. The post-annealing temperature and duration-control-related data

Fig. 1. Fabrication of Ru-doped NiMnB spherical cluster pillar (SCP) electrocatalysts along with Ru concentration variation and post-annealing duration variation as labelled. (a)–(d) SEM micrographs of Ru/NiMnB electrocatalysts with different Ru concentrations as labelled. (e)–(e-4) EDS top-view maps of single Ru/NiMnB particle. (f)–(f-3) Corresponding EDS line profiles of Ru Lγ, Ni Lα, Mn Lγ and B Kα phases. (g)–(j) Ru/NiMnB electrocatalysts at different post-annealing durations. (k)–(k-3) Raman analysis of electrocatalysts and corresponding contour plots of Raman bands.

can be found in Figs. S25–S31. To check the overall crystallinity, the Raman analysis was adapted as seen in Fig. 1(k). The Ru/NiMnB commonly demonstrated Raman bands at 134, 178, 632, 673 and 1024 cm^{-1}. The 30-min annealed Ru/NiMnB demonstrated the strongest peak intensities as clearly seen in the contour plots in Fig. 1(k-1)–(k-3), indicating the best crystallinity in this set. A more detailed Raman discussion can be found in supplementary text S-1.6. In addition, the before/after post-annealing characterizations are provided in Figs. S32–S34 and the post-annealed Ru/NiMnB demonstrated improved physical and electrochemical properties.

Fig. 2 shows structural characterizations of the best Ru/NiMnB electrocatalyst with TEM, EDS, XRD and XPS analysis. The high-

resolution TEM was conducted on microns-deep inside Ru/NiMnB SCPs after the FIB preparation as seen in Fig. 2(a)–(a-1). The TEM analysis indicated that the initially developed NiMnB possesses a polycrystal structure. Further, the Ru atoms were successfully dispersed within the NiMnB matrix as randomly oriented nanocrystals. For example, the lattice spacings of 0.308, 0.154 and 0.248 nm can be attributed to the NiMnB phases as shown in Fig. 2(a-1). At the same time, the interplane distances of 0.135 and 0.121 nm can correspond to Ru nanocluster phases. This indicated that the Ru atoms were successfully incorporated into the NiMnB matrix under a high-pressure and temperature hydrothermal reaction approach. Additional high-resolution TEM from
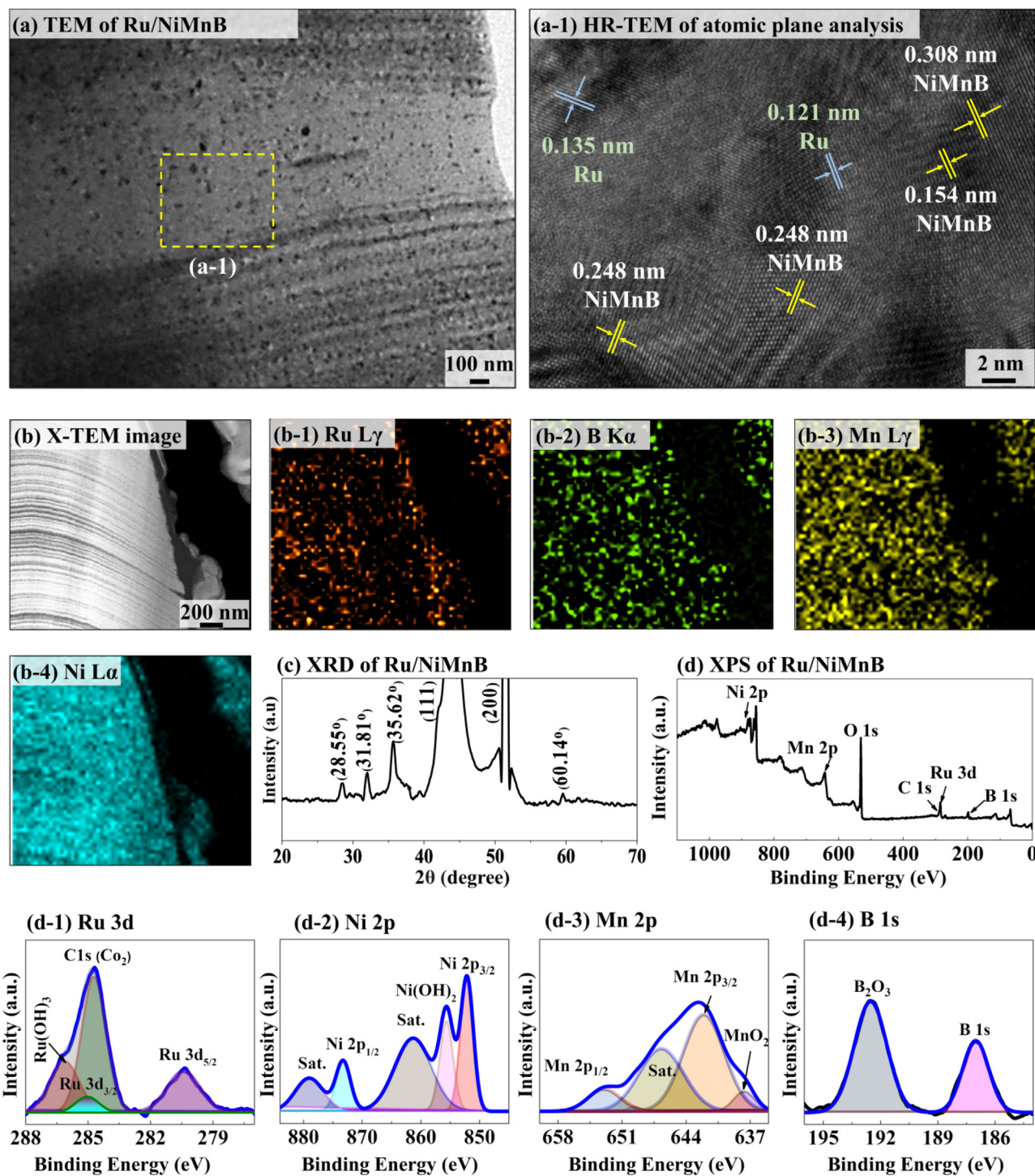
Fig. 2. Physical analyses on the best Ru/NiMnB SCP electrocatalyst. (a)–(a-1) TEM images and atomic plane analysis of Ru/NiMnB. (b)–(b-4) Cross-sectional EDS side-view maps of Ru/NiMnB electrocatalyst. (c) XRD pattern of Ru/NiMnB. (d) XPS spectra of Ru/NiMnB electrocatalyst and zoom-in spectra of (d-1) Ru 3d, (d-2) Ni 2p, (d-3) Mn 2p and (d-4) B 1s.

different areas of Ru/NiMnB was also characterized in Fig. S35 and showed polycrystal pattern consistency with various interplanar distances. The specific crystallographic planes were not identified due to polycrystal properties. Overall, the TEM analysis demonstrated that the Ru/NiMnB SCPs surface was composed of many small crystal domains and polycrystalline features in the internal structure evolution. The cross-sectional (CS) maps further validated the successful existence of Ru, Ni, Mn and B elements as shown in Fig. 2(b)–(b-4). While the Ru count was less, it showed

uniform distribution even at micron-deep internal structure as shown in Fig. 2(b-1). Further, the Ru/NiMnB was analyzed by X-ray diffraction (XRD) characterization as in Fig. 2(c). The strong diffraction peaks were identified around $2\theta = 43°$ and $52°$, which can be attributed to Ni $(1\,1\,1)$ and $(2\,0\,0)$ plane [27]. Smaller diffraction peaks were observed at 28.55, 31.81, 35.62, 37.21 and 60.14°. The multi-pole diffraction peaks also indicated the polycrystalline phase composition, which is consistent with TEM analysis. The bare NiMnB and Ru/NiMnB XRD patterns along with the PDF cards

of close materials systems are compared in Fig. S36. Initially, the NiMnB exhibited polycrystal phase, which can offer promising diffusion kinetics as a catalytic substrate [28] and then Ru was incorporated as nano cluster phase. The XRD diffraction patterns of NiMnB or Ru/NiMnB were not found in the literature or database and they did not match with the close systems likely due to the polycrystalline nature. A more detailed XRD analysis can be found in supplementary text S-1.7. Indeed, recent studies suggest that the polycrystalline structure can perform over single-crystal counterparts because of increased active sites, structural flexibility and stability [28,29].

The X-ray photoelectron spectroscopy (XPS) analysis was conducted as seen in Fig. 2(d)–(d-4). The full scan XPS survey spectrum showed Ru, Ni, Mn, B, C and O elemental peaks as seen in Fig. 2(d). The O and C peaks were observed from surface oxidation and binding energy (BE) calibration. The elemental BEs of nickel (Ni $2P_{1/2}$), manganese (Mn $2P_{1/2}$), boron (B 1s) and ruthenium (Ru $3d_{5/2}$) peaks were located at 873.2, 652.8, 192.5 and 280.3 eV respectively as shown in Fig. 2(d-1)–(d-4). The pristine elemental peaks of Ni $2P_{1/2}$, Mn $2P_{1/2}$, B 1s and Ru $3d_{5/2}$ can be found at 873.5, 652, 187.2 and 280.0 eV in the XPS handbook [30]. In the Ni 2p spectrum, the Ni $2P_{1/2}$ peak was shifted negatively by 0.3 eV from the elemental position, implying the reception of electrons. The change in elemental BEs can demonstrate the donating/receiving electrons for electronic interaction. Further, the characteristic Ni $2P_{3/2}$ peak also shifted by 0.5 eV negatively (from 852.6 to 852.1 eV), suggesting electron acceptance. The Ni(OH)$_2$ peak was found at 852.6 eV due to the adsorption of hydroxide groups and can transform into NiOOH (Ni^{3+}) [31]. The Ni satellite peaks were located at 878.5 and 861.4 eV [32]. The Mn $2P_{1/2}$ and Mn $2P_{3/2}$ peaks were observed at 651.9 and 641.5 eV in the Mn spectrum as shown in Fig. 2(d-3). Similarly, both Mn peaks were shifted to the lower BE (from 652 and 642.6 eV pristine), suggesting electron acceptance. The characteristic MnO$_2$ and satellite peaks were identified at 637.5 and 646.6 eV [33]. In addition, the B 1s peak was shifted positively by 0.2 eV from 188 eV elemental position as seen in Fig. 2(d-4), indicating the electron donation. The peak located at 192.5 eV assigned to B$_2$O$_3$ species. Considering all the BE shifts of elements, the B atoms might have donated electrons to the empty d-orbitals of Ni and Mn for NiMnB formation with strong ionic interaction. According to Pauling's theory, the electronegativity of B is 2.04, which is higher than Ni (1.91) and Mn (1.55). Thus, B could supply electrons to the metallic atoms for NiMnB growth [34]. The TEM and XRD analyses also revealed NiMnB exists in the polycrystalline phase and Ru atoms are incorporated as degree of nano-cluster. Meanwhile, the Ru $3d_{5/2}$ peak was positively shifted by 0.3 eV to the higher BE as shown in Fig. 2(d-1), indicating the electron supply. The Ru $3d_{3/2}$ peak was observed at 284.8 eV and shifted 0.72 eV positively from the elemental position of 284.08 eV, which suggested the successful Ru doping in the NiMnB matrix. The BE shift of Ru $3d_{5/2}$ and Ru $3d_{3/2}$ peaks demonstrated enhanced electron hot spots around the NiMnB matrix and may optimize electronic structure [35]. In this case, the minorly shifted BE of Ru species may be due to lattice strains and charge redistribution [36]. The strong electrostatic interaction can be beneficial to accelerate intrinsic activity, active site accessibility and H$_2$O dissociation capability [36]. In addition, the Ru(OH)$_3$ peak was identified at 286.12 eV from hydroxide (OH$^-$) ion adsorptions of metallic Ru species [29]. The C 1s peak was located at 284.62 eV from the BE calibration [35]. Overall, the XPS analysis further demonstrated that Ru species have been successfully incorporated into the NiMnB matrix, which can enhance electrochemical properties. A more detailed XPS analysis discussion of Ru/NiMnB can be found in supplementary text S-1.8.

3.2. Electrochemical OER and HER properties

Fig. 3 shows the electrochemical OER/HER properties of Ru/NiMnB SCP electrocatalysts with post-annealing optimization. Electrochemical impedance spectroscopy (EIS) was conducted in 1 M KOH to assess charge transfer ability as shown in Fig. 3(a) and (f). The 30-min annealed Ru/NiMnB demonstrated the smallest semicircle with the lowest OER/HER charge transfer resistance (R$_{ct}$) of 36.3 and 29.6 Ω in the EIS plots. The smallest impedance indicates the fastest ion transportation kinetics, which could facilitate desirable catalytic performance [32,37]. The double-layer capacitance (C$_{dl}$) values were investigated in the non-faradaic region of cyclic voltammetry (CV) curves as shown in Fig. 3(b) and (g). The 30-min Ru/NiMnB showed the highest OER/HER C$_{dl}$ values of 4.8 and 4.1 mF/cm^2, suggesting the largest electrochemical surface area (ECSA). The 30-min Ru/NiMnB exhibited the highest OER/HER ECSA of 30 and 25.62 cm^2 as summarized in Fig. S30, which can facilitate effective interaction between the electrode and intermediates with the highest number of active sites [37]. In addition, the C$_{dl}$ value is proportional to the ECSA and the high ECSA can provide more active sites, faster interfacial interaction and reduced energy barrier for OER/HER [29,37]. Further, the C$_{dl}$ value, ECSA and LSV performances between bare NiMnB and Ru/NiMnB were compared in Fig. S41. The Ru clusters significantly enlarged the ECSA by exposing more accessible active sites as compared to bare NiMnB: i.e., OER/HER ECSA of 19.37 and 18.12 cm^2 in Figs. S41(c)–41(d), indicating superior intrinsic activity of Ru/NiMnB. The related CV curves corresponding to C$_{dl}$ and ECSA values are provided in Figs. S28–S30 and S40. The Tafel slopes were taken from the linear portion of liner sweep voltammetry (LSV) curves based on the relation: η = b log|j| + a, where the Tafel slope and current density defined with b and j as shown in Fig. 3(c) and (h) [25]. The 30-min Ru/NiMnB demonstrated the lowest OER/HER Tafel slope values of 76 and 66 mV/dec, indicating rapid and favorable reaction kinetics [25].

The OER/HER performance of post-annealed Ru/NiMnB samples was evaluated in 1 M KOH as shown in Fig. 3(d) and (i). The 30-min annealed Ru/NiMnB exhibited the highest OER/HER performances in linear sweep voltammetry (LSV) curves. It showed the lowest overpotential of 390 and 230 mV at 300 mA/cm^2 as summarized in Fig. 3(d-1)–(i-1). This result suggested significant improvement over the bare NiMnB SCPs (550 and 294 mV at 300 mA/cm^2 for OER/HER in Fig. S4) and the overpotentials are reduced by 160 and 64 mV respectively at 300 mA/cm^2 with unique Ru nanoclusters incorporation. The summarized OER/HER overpotentials demonstrated volcanic curves' relationship with applied annealing duration, indicating an optimum annealing can maximize the catalytic performance. The proper annealing conditions can offer higher crystallinity, conductivity and activation of inactive sites, facilitating better electron transfer and mass transport [16]. On the other hand, excessive thermal annealing can cause phase segregation by destroying sub-nano structures and structural degradation, which is reflected in higher overpotentials and lower catalytic efficiency [16]. The OER reaction mechanism can be given as follows, the (iii) and (iv) steps are considered to be rate-determining steps (RDS): (i) M+OH$^-$ → M-OH* + e$^-$, (ii) M-OH* + OH$^-$ → M-O* + H$_2$O+e$^-$, (iii) 2 M-O* + OH$^-$ → 2 M+O$_2$ or M-O* + OH$^-$ → M-OOH* + e$^-$, (iv) M-OOH* + e$^-$ → M+O$_2$ + H$_2$O +e$^-$, where the M is the metallic active sites and M-OH, M-O, M-OOH are reaction intermediates [11,38]. On the other hand, HER reaction mechanism can be summarized as M+H$_2$O+e$^-$ → M-H* + OH$^-$ (Volmer step), M-H* + H$_2$O+e$^-$ → M+OH$^-$ + H$_2$ (Heyrovsky step) or as 2 M-H* → 2 M+H$_2$ (Tafel step) [38]. The Ru incorporation is key to facilitating the rapid conversion of H$_{ad}$ and adsorption/release of hydroxyl species towards improved OER/HER [29,37]. The OER reaction kinetics mostly depend on RDS steps
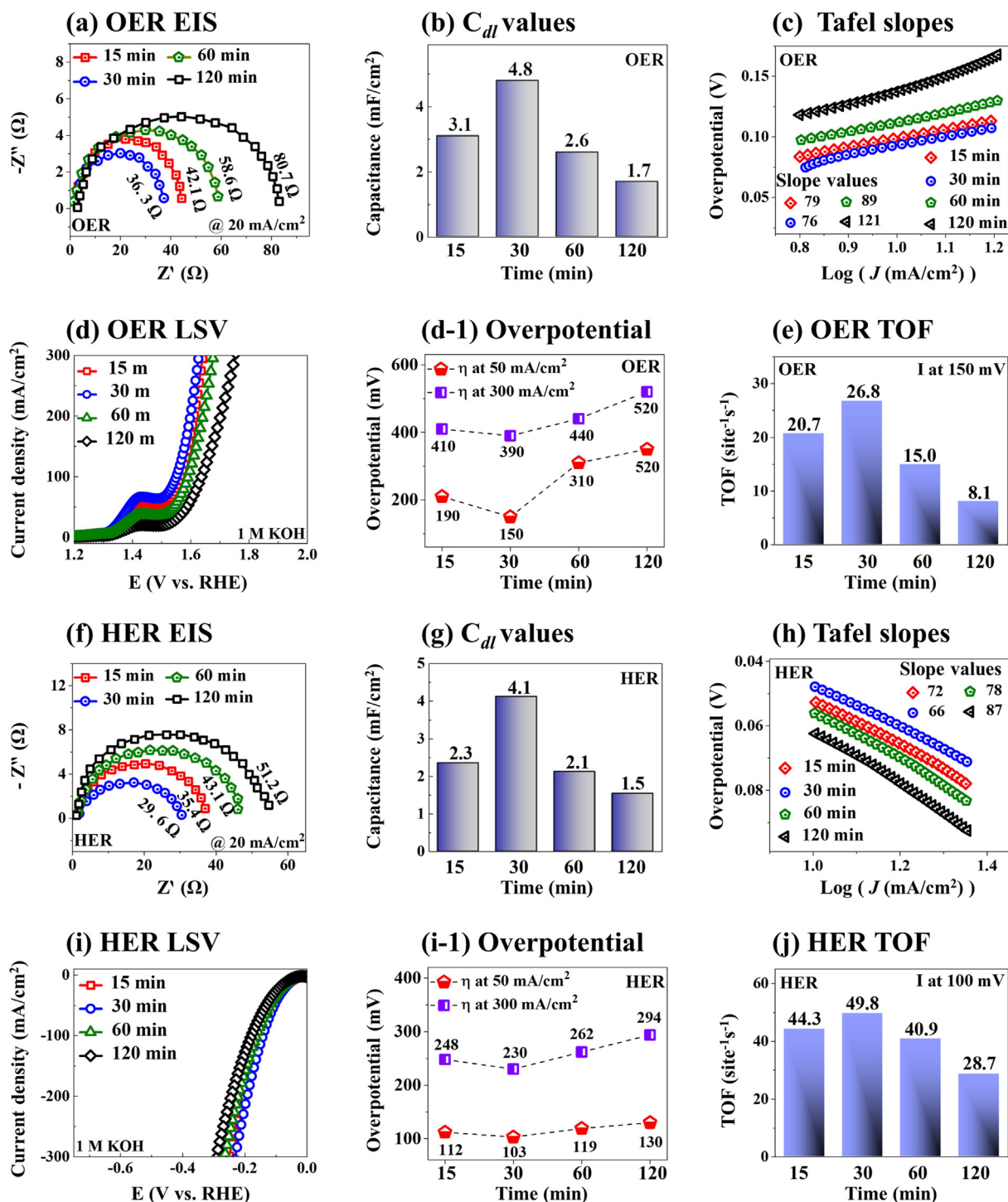
Fig. 3. Three electrode (3-E) electrochemical properties of Ru/NiMnB with post-annealing duration variation set in 1 M KOH. (a, f) OER/HER EIS plots of Ru/NiMnB. (b, g) double-layer capacitance (C_{dl}) values. (c, h) Tafel plots and slope values. (d, i) Three electrode (3-E) OER/HER LSV curves. (d-1, i-1) Corresponding overpotential at 50 and 300 mA/cm^2. (e, j) TOF values.

[39,40]. The breaking of M-OH bonds plays a crucial role in faster kinetics and is involved in the RDS step [41]. The highly concentrated M-O* (Ru–O) with Ru nanocluster incorporation could accelerate OER kinetics [39]. Further, the HER Tafel result indicated that HER RDS was accelerated by Volmer-Heyrovsky steps [42]. Ru doping could offer a faster Volmer step for favorable H$_2$ evolution kinetics [39,43]. Also, the optimized metal hydride (Ru–H) bond formation can facilitate rapid H* adsorption to improve HER [43]. Overall, Ru-doping plays a considerable role in enabling the speedy

diffusion of reaction intermediates and improving electrochemical properties [37,44]. The OER/HER performance of Ru/NiMnB is compared with bare Ni foam (NF) as seen in Fig. S43. A more detailed discussion about Ru doping's effect on NiMnB towards enhanced ECSA and improved OER/HER performances are provided in supplementary text S-1.13. Further, the redox peak commonly appearing in OER LSV in Fig. 4(f) may be due to the transformation of metallic species into a high valance state [45]. The faster redox conversion of absorbed oxygenated intermediates of O*, OH* and
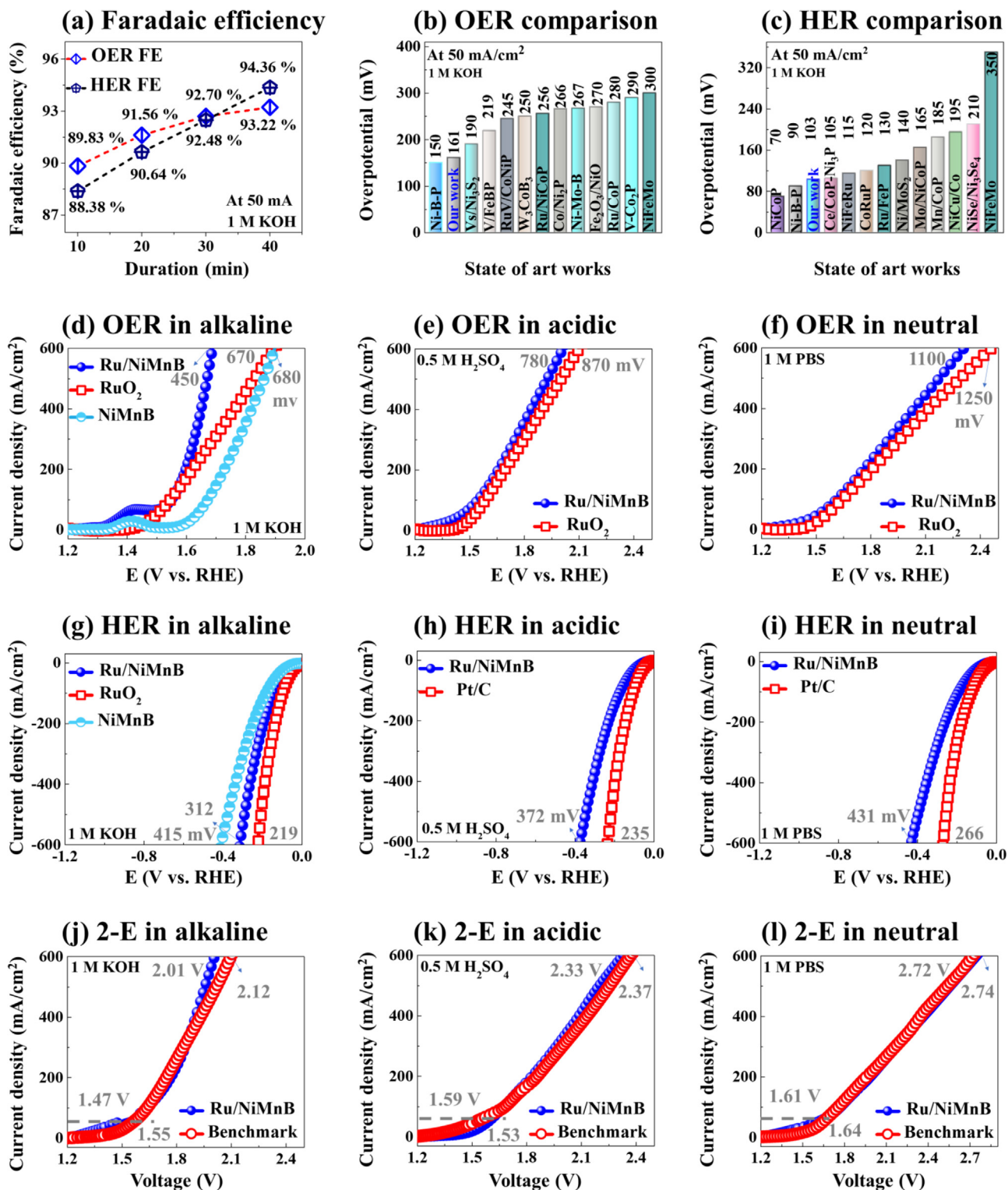
Fig. 4. Faradaic efficiency (FE), OER/HER state-of-the-artwork comparisons, 3-E OER/HER and 2-E LSV in different pH solutions. (a) FE measurement of the best Ru/NiMnB. (b, c) OER/HER performance comparison with the state-of-the-art (Related to Tables 1 and 2). (d)–(i) OER/HER LVS in different pH solutions compared with the benchmark electrocatalysts of RuO$_2$ and Pt/C. (j)–(l) 2-E LSV in different pH solutions.

OOH* may also be beneficial to lower the sluggish kinetics of RDS and facilitate excellent OER activity [40,45]. The OER CV scan of Ru/NiMnB was performed to better understand the OER mechanism in Fig. S37 and a more detailed discussion can be found in supplementary text S-1.9.

Further, the turnover frequency (TOF) was investigated to understand the intrinsic activity of electrocatalysts as shown in Fig. 3(e) and (j). The 30-min Ru/NiMnB exhibited the highest OER/HER TOF values of 26.8 and 49.8 site-s^{-1}, suggesting the highest intrinsic properties and faster O$_2$/H$_2$ generations. The loading

mass of Ru/NiMnB and bare NiMnB were 0.6 and 0.4 mg/cm^2. The calculated active sites of each catalyst are based on considering the presence of all metallic species. To evaluate the loading effect, the TOF values were compared in Fig. S42 and the Ru/NiMnB demonstrated a significantly high O$_2$/H$_2$ generation rate over NiMnB. A more detailed TOF-related calculation can be found in supplementary text S-1.10. Faradaic efficiency (FE) is a key factor in evaluating the catalyst's charge transfer efficiency for practical application. Further, the FE measurement was conducted at 50 mA/cm^2 in 1 M KOH as shown in Fig. 4(a). The Ru/NiMnB demonstrated 93.22 and 94.36% of O$_2$ and H$_2$ evolution efficiency, indicating no obvious side reaction and excellent conversation rates. The FE values demonstrated the acceptable range for practical application by spontaneous reaction and avoiding gas recombination on the electrode surface. A more detailed discussion on the FE measurement can be found in supplementary text S-1.11 with Fig. S44. Finally, the OER/HER performances of Ru/NiMnB SCPs are compared with the state-of-the-art reported works at 50 mA/cm^2 in 1 M KOH in Fig. 4(b) and (c). The Ru/NiMnB demonstrated highly comparable OER/HER, establishing Ru/NiMnB as a promising candidate for efficient water splitting. Additional comparison information can be found in Tables 1 and 2. Overall, the 30 min-Ru/NiMnB demonstrated the best OER/HER performance in this set. The improved performance of Ru/NiMnB can be attributed to well-designed spherical cluster pillar morphology, enlarged surface area, abundant active sites and high intrinsic activity [36,46]. The Ru incorporation in NiMnB can modulate electronic configuration and reduce charge transfer resistance by optimizing the adsorption/desorption capacity [36,46]. The summarized OER/HER properties of the best Ru/NiMnB SCPs are provided in Table S1.

3.3. Different pH performance of Ru/NiMnB

The OER/HER performance of Ru/NiMnB SPCs was compared to the benchmark electrocatalysts in different pH electrolytes as shown in Fig. 4(d)–(i). Alkaline (1 M KOH, pH $\sim$ 14), acidic (0.5 M H$_2$SO$_4$, pH $\sim$ 0), and neutral (1 M PBS, pH $\sim$ 7.4) were adapted as different pH solutions. For comparisons, RuO$_2$ and Pt/C were adapted as OER/HER benchmarks and bare NiMnB performance was included in 1 M KOH LSV plots. The OER/HER overpotential values of Ru/NiMnB were reduced 220/103 mV at 600 mA/cm^2 in 1 M KOH as seen in Fig. 4(d) and (g), clearly demonstrating Ru doping effect. The Ru/NiMnB SCPs demonstrated better OER than the RuO$_2$ and HER performance was slightly lower than the Pt/C benchmark in all pH media as shown in Fig. 4(d)–(i). The Ru/NiMnB SCPs showed super-lower OER overpotentials of 450, 780 and 1,100 mV at 600 mA/cm^2 high current density respec-

tively in 1 M KOH, 0.5 M H$_2$SO$_4$ and 1 M PBS as compared to the RuO$_2$ values of 670, 780 and 1250 mV as seen in Fig. 4(d)–(f), indicating significantly higher OER capabilities. In addition, the Ru/NiMnB exhibited HER overpotentials of 312, 372 and 431 mV at 600 mA/cm^2 in different pH media as shown in Fig. 4(g)–(i). Overall, the OER/HER performance is much higher in alkaline media due to its high solution conductivity and favorable reaction environments [25,47]. The Ru/NiMnB demonstrated a significantly high O$_2$/H$_2$ generation rate in 1 M KOH as compared to the benchmarks in Fig. S45. Thus, the commercial electrolyze commonly adapts the alkaline medium for large-scale H$_2$ production [47]. On the other hand, the high concentration of protons (H$^+$) can decompose active species of TM-based electrocatalysts in acidic electrolytes [12,26]. The Ru/NiMnB demonstrated a promising response in harsh acidic solutions due to strong anti-corrosion properties [16,48]. In addition, neutral media is benign and exhibits a higher energy barrier, which can limit the rate of water oxidation [49,50]. The neutral solution performance of Ru/NiMnB and benchmark are both lower as compared to the other media due to the slow interfacial charge/proton transfer rate and slight heat generation during electrolysis [49]. However, neutral electrolytes are environmentally harmless and extremely important for green H$_2$ generation. Further, the pH level of 1 M PBS is $\sim$7.4, which is nearly the same as natural seawater water. Thus, Ru/NiMnB can possess high potential in natural waters.

Further, the chronoamperometry (CA) test of Ru/NiMnB SCPs demonstrated steady-state stable current response at various applied voltages for OER/HER as shown in Fig. S38. The CA and LSV comparisons show a good agreement, indicating smooth formation/release of gas bubbles [51]. After 1,000 cyclic CV operations (scan rate 100 mV/s) over 10 h, no obvious change is observed in LSV curves as shown in Fig. S39, indicating high HER/OER repeatability. Overall, the Ru/NiMnB SCPs exhibited superior catalytic activity, repeatability and stability under all pH conditions. Inspired by the exceptional OER and HER activity, we have configured a bifunctional two-electrode (2-E) system consisting of Ru/NiMnB as both anode and cathode (Ru/NiMnB (+) || Ru/NiMnB (−)) for overall water splitting (OWS). The bifunctional Ru/NiMnB outperformed the benchmarks of RuO$_2$ (+) || Pt/C (−) in all pH solutions as shown in Fig. 4(j)–(l). Generally, the industry utilizes 2-E system OWS and high current operation for cost-effective hydrogen production. Stable high-current operation is required to meet industrial requirements [49]. The Ru/NiMnB demonstrated low cell voltages of 2.01, 2.33 and 2.74 V at 600 mA/cm^2 respectively in 1 M KOH, 0.5 M H$_2$SO$_4$ and 1 M PBS as compared to the benchmark values of 2.12, 2.37 and 2.72 V in Fig. 4(j)–4(l). Generally, Ru/NiMnB demonstrated highly comparable performances in all pH media

Table 1
Comparison of OER performance with the state-of-art electrocatalysts at 50, 100 and 600 mA/cm^2 current density in 1 M KOH.

	OER Overpotential [mV] 50 at mA/cm^2	OER Overpotential [mV] 100 at mA/cm^2	OER Overpotential [mV] 600 at mA/cm^2	Year	Reference
Ni-B-P	150	290	Not available	2023	[12]
Ru/NiMnB	**161**	**320**	**450**	**Our work**	**Our work**
Vs-Ni$_3$S$_2$	190	330	Not available	2024	[56]
V/FeBP	219	258	432	2022	[26]
RuV/CoNiP	245	260	Not available	2021	[57]
W$_3$CoB$_3$	250	310	Not available	2022	[16]
Ru/NiCoP	256	265	Not available	2022	[36]
Co/Ni$_2$P	266	274	Not available	2022	[58]
Ni-Mo-B	267	360	490	2022	[25]
Fe$_2$O$_3$/NiO	270	281	Not available	2022	[59]
Ru/CoP	280	350	Not available	2023	[60]
V-Co$_2$P	290	320	Not available	2023	[61]
NiFeMo	300	410	Not available	2023	[62]

Table 2
Comparison of HER performance with the state-of-art electrocatalysts at 50, 100 and 600 mA/cm^2 current density in 1 M KOH.

	HER Overpotential [mV] 50 at mA/cm^2	HER Overpotential [mV] 100 at mA/cm^2	HER Overpotential [mV] 600 at mA/cm^2	Year	Reference
NiCoP	70	115	220	2023	[63]
Ni-B-P	90	139	Not available	2023	[12]
Ru/NiMnB	**103**	**141**	**312**	**Our work**	**Our work**
Ce/CoP-Ni$_3$P	105	140	210	2023	[64]
NiFeRu	115	190	Not available	2023	[65]
CoRuP	120	150	Not available	2023	[66]
Ru/FeP	130	185	Not available	2022	[67]
Ni/MoS$_2$	140	243	Not available	2021	[68]
Mo/NiCoP	165	195	Not available	2023	[69]
Mn/CoP	185	300	Not available	2022	[70]
NiCu/Co	195	220	320	2023	[71]
NiSe/Ni$_3$Se$_4$	210	235	Not available	2022	[72]
NiFeMo	350	430	Not available	2023	[62]

and the lower overpotential at high current seems promising. The different pH performances of Ru/NiMnB are summarized in Table S2.

3.4. High current performance and post-electrocatalytic characterizations

Fig. 5 shows the 2-E overall water splitting (OWS) performances of Ru/NiMnB in various conditions. First, the bifunctional Ru/NiMnB (+, −) exhibited significantly higher 2-E performance over the RuO$_2$ (+) || Pt/C (−) up to 2,000 mA/cm^2 high current density in 1 M and 6 M KOH solutions as shown in Fig. 5(a). This efficient OWS performance of Ru/NiMnB is likely assigned to the highly efficient active sites and enhanced intrinsic conductivity. The bifunctional Ru/NiMnB demonstrated a low cell voltage of 2.80 V at 2,000 mA/cm^2 in 1 M KOH, surpassing the benchmark value of 3.22 V. Further, the Ru/NiMnB exhibited lower cell voltages of 2.18 and 2.75 V respectively at 1,000 and 2,000 mA/cm^2 in 6 M KOH at 60 °C of industrial operational conditions. The 6 M high-concentration alkalinity (K$^+$ and OH$^−$) can offer lower solution resistance and faster ion transportation [13,52]. Also, the higher temperature facilitates favorable reaction thermodynamics by lowering the kinetic energy barrier of the electrolysis process [13,52]. The bifunctional Ru/NiMnB response demonstrated stable currents at various CA operational voltages in 1 M KOH and minor differences between CA/LSV comparisons confirmed spontaneous reactions as shown in Fig. 46. The Ru/NiMnB demonstrated nearly the same performance after running 1,000 cycles of CV (over ~10 h) in 1 M KOH as presented in Fig. 5(b), indicating excellent repeatability. Along with performance, long-term high current durability is a crucial factor for large H$_2$ production. More attractively, the Ru/NiMnB exhibited superior stability at 1,000 mA/cm^2 in 6 M KOH (at 60 °C) for 150 h (over 6 days) to meet harsh industrial conditions as shown in Fig. 5(c). This confirmed the strong corrosion resistance and mechanical robustness of Ru/NiMnB SCPs for high-current and long-term operation. The bifunctional WS performance is compared with recent state-of-the-art works in 1 M KOH as presented in Fig. 5(d) and Table 3. In addition, the OWS performance of Ru/NiMnB is highly comparable to that of advanced reported electrocatalysts in alkaline media. The high anodic OER capability of Ru/NiMnB played a key role in superior 2-E OWS performances [47].

The post-stability physical and electrochemical characterizations were investigated with SEM, Raman, XRD, XPS and LSV analyses after 1,000 mA/cm^2 high current stability in 1 M KOH for 12 h as shown in Figs. S48–S51. In this work, the anodic capability of Ru/NiMnB is highly promising. To get deeper insights into Ru/NiMnB, all post-stability physical characterizations were performed on an

anodic OER electrode. The Ru/NiMnB SCPs exhibited a slightly rougher surface and well-preserved spherical morphology as shown in Fig. S48(a), indicating strong morphological robustness. The post-stability Raman spectrum showed slightly lower peak intensity and additional peaks at ~465, 600 and 820 cm$^{−1}$ as shown in Fig. S48(b). The observed peaks at ~465 and 600 cm$^{−1}$ can be attributed to NiO and NiOOH oxide species formation due to unavoidable Ni^{+2} to Ni^{+3} conversion during high current redox reactions [53]. Indeed, metallic species transformation (M-OH$_{ad}$ + OH$^−$ → MOOH+H$_2$O+e$^−$) can facilitate fast ions diffusion, active sites and stability [53]. Also, the post-stability XRD maintained most of the major diffraction peak positions as shown in Fig. S48(c), indicating the maintenance of the stable crystal structure. However, the reduced diffraction peak intensities are likely due to surface oxide formation and the adsorption of hydroxide (OH$^−$) ions, indicating an involvement of the surface elements and participation in the WS reaction. The post-stability high-resolution XPS spectra of Ru/NiMnB are shown in Figs. S48(d-1)–(d-4). Generally, the elemental peaks were sharply reduced, while the oxide states were largely increased due to partial oxidation of the surface under alkaline reactions [54]. Further, the full-scan XPS indicated the co-existence of active materials as shown in Figs. S48 (d) and S49. In addition, the post-stability electrochemical performance of Ru/NiMnB electrocatalysts (used as anode and cathode for OER and HER) demonstrated nearly the same OER/HER and OWS activity as seen in Figs. S50 and S51, suggesting excellent electrochemical robustness. Additionally, the full scan XPS and maintenance of electrochemical performance confirmed the retention of the doped Ru. Further, the 100-hour stability test at 1,000 mA/cm^2 was performed in 1 M KOH as illustrated in Fig. S52. The post-stability electrode content of Ru/NiMnB was characterized and compared with fresh sample using EDS spectra and quantitative elemental determination as shown in Fig. S53. The EDS spectra confirmed the exitance of all materials and quantitative analysis showed a slight variation in elemental contents ratios, indicating only a slight amount of element may form the surface oxide/hydroxide, contributing to active site formation and stable operation. Overall, all the post-stability characterizations demonstrated promising and robust material properties.

3.5. Hybrid performance and natural water application

Along with the superior anodic OER activity of Ru/NiMnB, the hybrid system is configured by coupling with the conventional Pt/C, i.e., Ru/NiMnB (+) || Pt/C (−). The Ru/NiMnB hybrid configuration largely outperformed the benchmarks in 1 M KOH as seen in Fig. 5(e). The hybrid demonstrated a low cell voltage of 2.23 V at 2,000 mA/cm^2 as compared to the benchmark values of 3.22 V. This
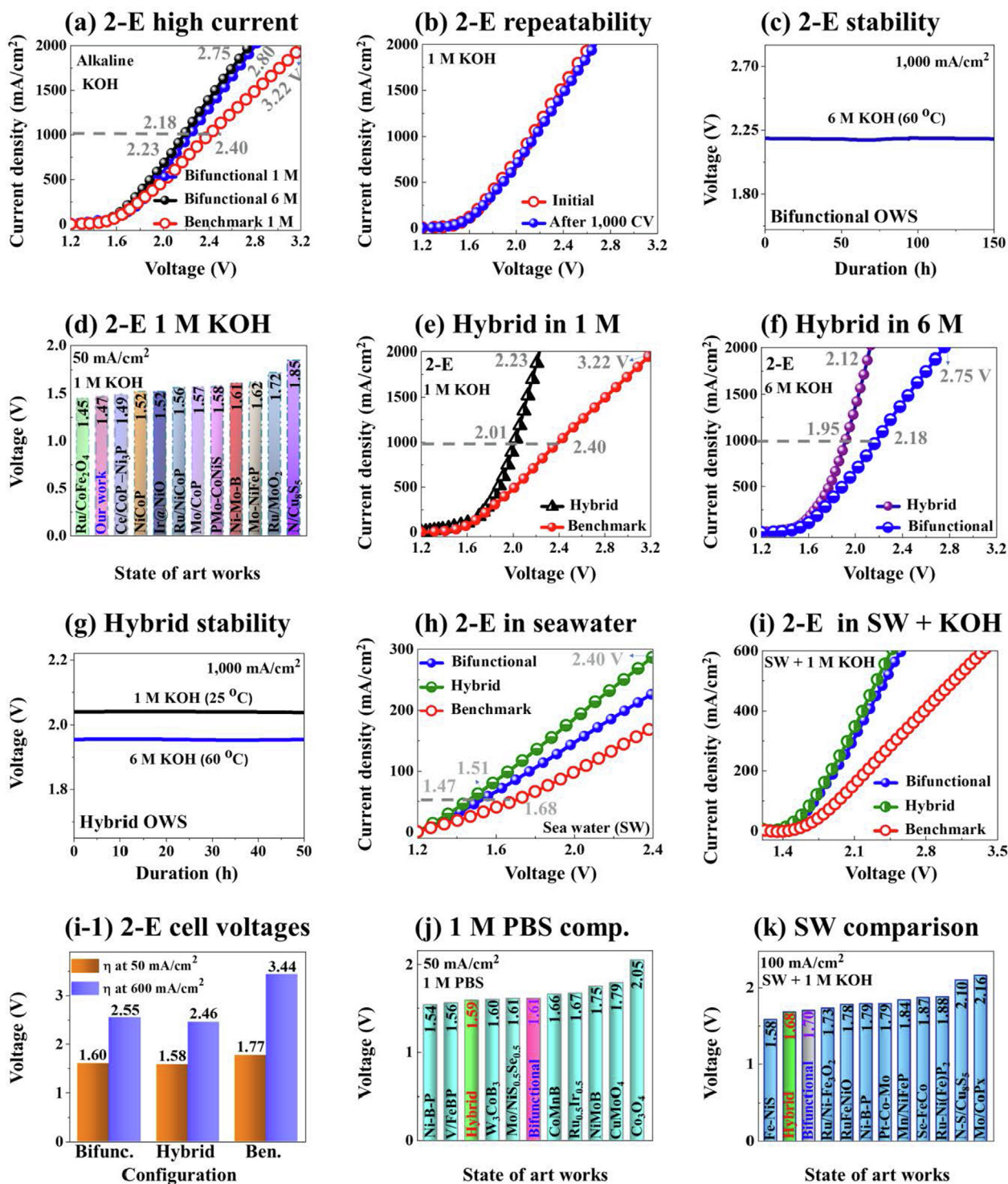
Fig. 5. 2-E LSV activity of Ru/NiMnB under various conditions. (a) 2-E in 1 M and 6 M KOH. (b) 2-E repeatability. (c) 2-E stability test. (d) 2-E comparison in 1 M KOH (Related to Table 3). (e) 2-E hybrid (Ru/NiMnB(+) || Pt/C(−)) LSV in 1 M KOH. (f) 2-E LSV in 6 M KOH. (g) Stability test of hybrid configuration. (h) Bifunctional, hybrid and benchmark performance in seawater (SW). (i) 2-E in SW+1 M KOH. (i-1) Potential at 50 and 600 mA/cm². (j, k) 2-E comparison in 1 M PBS and SW+1 M KOH (Related to Tables S5 & S6).

suggests that Ru/NiMnB can be a cost-effective and high-performing anodic replacement for RuO₂. Further, the hybrid system exhibited a super-low cell voltage of 2.12 V at 2,000 mA/cm² in 6 M KOH at 60 °C under industrial conditions. The hybrid demonstrated multi-step stability at 1,000 mA/cm² in both 1 M and 6 M KOH over 100 h as shown in Fig. 5(g), confirming configurational high current stability. In addition, the hybrid outperformed the benchmarks in all pH solutions as seen in Fig. S54.

Further, the hybrid system showed stable CA performance under various operational voltages as provided in Fig S55. A summary of the high current and different pH OWS performance of Ru/NiMnB configuration can be found in Tables S3–S4.

Inspired by the promising 1 M PBS neutral media performance, the OWS operation was conducted in bare natural seawater (SW) and alkaline seawater (SW+1 M KOH) as shown in Fig. 5(h)–(i). The hybrid and bifunctional Ru/NiMnB systems demonstrated bet-

Table 3

Comparison of overall water splitting (OWS) performance with the state-of-art electrocatalysts at 50, 100 and 500 mA/cm^2 density in 1 M KOH.

	2-E Potential [V] 50 at mA/cm^2	2-E Potential [V] 100 at mA/cm^2	2-E Potential [V] 500 at mA/cm^2	Year	Reference
Ru/CoFe$_2$O$_4$	1.45	1.60	Not available	2023	[73]
Ru/NiMnB	**1.47**	**1.63**	**1.95**	**Our Work**	**Our Work**
Ce/CoP-Ni$_3$P	1.49	1.62	1.78	2023	[64]
NiCoP	1.52	1.65	1.81	2023	[63]
Ir@NiO	1.52	1.56	Not available	2024	[74]
Ru/NiCoP	1.56	1.78	Not available	2022	[36]
Mo/CoP	1.57	1.61	Not available	2023	[75]
PMo-CoNiS	1.58	1.64	Not available	2024	[76]
Ni-Mo-B	1.61	1.76	2.18	2022	[25]
Mo-NiFeP	1.62	1.66	1.82	2023	[77]
Ru/MoO$_2$	1.72	1.88	Not available	2021	[78]
N/Cu$_8$S$_5$	1.85	1.96	Not available	2023	[79]

ter performance over the benchmarks in real seawater (SW) as shown in Fig. 5(h), where the hybrid exhibits only 2.40 V at 300 mA/cm^2. Both bifunctional and hybrid systems of Ru/NiMnB largely outperformed the benchmarks in alkaline seawater (SW +1 KOH) as illustrated in Fig. 5(i). The hybrid system demonstrated only 2.46 V at 600 mA/cm^2 and surpassed the 3.44 V values of the benchmarks as summarized in Fig. 5(i-1), indicating excellent natural water electrolysis capabilities. The 1 M KOH was introduced in natural water to reduce solution resistance and faster H$_2$ production. Generally, the observed natural seawater performance is comparatively lower than freshwater due to various cations and anions such as Ca$^+$, Mg$^+$, F$^-$, Cl$^-$, Br$^-$, unexpected chemicals, biological elements and dust etc., which can make natural water electrolysis more challenging [55]. White perceptions were observed during the SW electrolysis, which may indicate the formation of Mg(OH)$_2$/Ca(OH)$_2$ [55]. Additionally, the Ru/NiMnB systems also largely surpassed the benchmarks in alkaline river water (RW+1 M KOH) as provided in Fig. S56. Further, hybrid and bifunctional systems maintained long stable operation at 300 and 500 mA/cm^2 in alkaline seawater (SW+1 KOH) as shown in Fig. S57, suggesting strong anti-corrosion resistance against unexpected ions, bacteria and micrograms. The neutral media and seawater performances of Ru/NiMnB are compared with recent state-of-the-art artworks in 1 M PBS and SW+1 KOH as shown in Fig. 5(j), (k) with Tables S5–S6. The highly comparable natural water performance of both Ru/NiMnB configurations clearly demonstrated that it can be one of the best promising electrocatalysts for natural water electrolysis.

4. Conclusions

In summary, the Ru/NiMnB spherical cluster pillar (SCP) electrocatalyst was successfully fabricated using a combined electrodeposition and scalable hydrothermal synthesis approach for high-performance multifunctional water electrolysis applications. Systematic optimization and characterizations verified that Ru doping in the NiMnB matrix collectively improves conductivity, electrochemical surface area and intrinsic activity, contributing to high-performance overall water splitting. The bifunctional Ru/ NiMnB SCP exhibited a low turnover cell voltage of 1.47 V at 50 mA/cm^2 in 1 M KOH and outperformed the benchmark up to a high current density of 2,000 mA/cm^2. Furthermore, continuous operation was demonstrated for over 150 h at 1,000 mA/cm^2 in 6 M KOH at 60 °C, meeting industrial conditions. Notably, the optimized spherical cluster morphology, enhanced electronic structure, and abundant active sites of the electrocatalyst make Ru/NiMnB particularly practical as an OER electrode. Alongside its excellent anodic characteristics, the prepared hybrid configuration delivered ultra-low cell voltages of 2.13 and 2.12 V at 2,000 mA/cm^2 in 1 M KOH and 6 M KOH (60 °C), respectively, with

stable operation. This work provides valuable insights into the construction of advanced and stable multifunctional electrocatalysts, significantly contributing to the future hydrogen economy.

Experimental section

Experimental details can be found in the supplementing Information.

CRediT authorship contribution statement

Md Ahasan Habib: Writing – review & editing, Writing – original draft, Investigation, Data curation. **Shusen Lin:** Investigation, Data curation. **Mehedi Hasan Joni:** Investigation, Data curation. **Sumiya Akter Dristy:** Investigation, Data curation. **Rutuja Mandavkar:** Investigation, Data curation. **Jae-Hun Jeong:** Supervision, Methodology, Investigation. **Jihoon Lee:** Writing – review & editing, Funding acquisition, Conceptualization.

Declaration of competing interest

The authors declare that they have no known competing financial interests or personal relationships that could have appeared to influence the work reported in this paper.

Acknowledgements

Appendix A. Supplementary material

Supplementary material to this article can be found online at https://doi.org/10.1016/j.jechem.2024.08.060.

References

[1] M. Kumar, N.K. Singh, K.B. Prajapati, R.S. Kumar, R. Singh, Transition Metal-Based Electrocatalysts: Applications in Green Hydrogen Production and Storage, ACS Publications, 2023, pp. 43–71.
[2] F. Yu, H. Zhou, Y. Huang, J. Sun, F. Qin, J. Bao, W.A. Goddard, S. Chen, Z. Ren, Nat. Commun. 9 (2018) 2551.
[3] S.Y. Tee, K.Y. Win, W.S. Teo, L.D. Koh, S. Liu, C.P. Teng, M.Y. Han, Adv. Sci. 4 (2017) 1600337.
[4] X. Zhu, D.C. Nguyen, S. Prabhakaran, D.H. Kim, N.H. Kim, J.H. Lee, Mater Today Nano 21 (2023) 100296.
[5] M.R. Kandel, U.N. Pan, P.P. Dhakal, R.B. Ghising, T.T. Nguyen, J. Zhao, N.H. Kim, J. H. Lee, Appl. Catal. B Environ. 331 (2023) 122680.
[6] G. Li, X. Qiao, Y. Miao, T. Wang, F. Deng, Small 19 (2023) 2207196.

[7] A.M.R. Ramírez, S. Heidari, A. Vergara, M.V. Aguilera, P. Preuss, M.B. Camarada, A. Fischer, ACS Mater Au 3 (2023) 177–200.

[8] J.L. Bian, Z.Y. Song, Y.Z. Zhang, C.W. Cheng, Mater. Today Nano 8 (2019) 100053.

[9] M.R. Kandel, U.N. Pan, D.R. Paudel, P.P. Dhakal, N.H. Kim, J.H. Lee, Compos. B Eng. 239 (2022) 109992.

[10] A. Li, L. Zhang, F. Wang, L. Zhang, L. Li, H. Chen, Z. Wei, Appl. Catal. B Environ. 310 (2022) 121353.

[11] G. Ma, J. Ye, M. Qin, T. Sun, W. Tan, Z. Fan, L. Huang, X. Xin, Nano Energy 115 (2023) 108679.

[12] M. Ahasan Habib, R. Mandavkar, S. Lin, S. Burse, T. Khalid, M. Hasan Joni, J.H. Jeong, J. Lee, Chem. Eng. J. 462 (2023) 142177.

[13] S. Lin, M.A. Habib, R. Mandavkar, R. Kulkarni, S. Burse, Y.U. Chung, C. Liu, Z. Wang, S. Lin, J.H. Jeong, J. Lee, Adv. Sustain. Syst. 6 (2022) 1–14.

[14] M. Yu, C. Weidenthaler, Y. Wang, E. Budiyanto, E. Onur Sahin, M. Chen, S. DeBeer, O. Rüdiger, H. Tüysüz, Angew. Chem. Int. Ed. 134 (2022) 202211543.

[15] G. Anandha Babu, S. Perumal, M.K.A. Mohammed, M. Govindasamy, A.A. Alothman, M. Ouladsmane, R. Ganesan, Int. J. Hydrogen Energy 54 (2024) 652–664.

[16] M.A. Habib, R. Mandavkar, S. Burse, S. Lin, R. Kulkarni, C.S. Patil, J.H. Jeong, J. Lee, Mater. Today Energy 26 (2022) 101021.

[17] Y. Yu, J. Li, J. Luo, Z. Kang, C. Jia, Z. Liu, W. Huang, Q. Chen, P. Deng, Y. Shen, X. Tian, Mater. Today Nano 18 (2022) 100216.

[18] J. Zhang, J. Lian, Q. Jiang, G. Wang, Chem. Eng. J. 439 (2022) 135634.

[19] X. Zhang, Y. He, B. Zhu, X. Wan, S. Hua, H. Tang, Int. J. Hydrogen Energy 48 (2023) 4686–4693.

[20] S. Guo, D. Xu, Y. Li, Y. Guo, S. Wang, D.D. Macdonald, J. Supercrit. Fluid 170 (2021) 105138.

[21] X. Tan, S. Chen, D. Yan, R. Du, Q. Zhong, L. Liao, Z. Tang, F. Zeng, J. Energy Chem. 98 (2024) 588–614.

[22] A.M. Butt, M. Batool, M.A. Jaoude, A. Qurashi, J. Electroanal. Chem. 937 (2023) 117393.

[23] M. Pal, U. Pal, J.M.G.Y. Jiménez, F. Pérez-Rodríguez, Nanoscale Res. Lett. 7 (2012) 1–12.

[24] T. Cui, J. Chi, J. Zhu, X. Sun, J. Lai, Z. Li, L. Wang, Appl. Catal. B Environ. 319 (2022) 121950.

[25] R. Mandavkar, A. Habib, S. Lin, R. Kulkarni, S. Burse, J. Jeong, J. Lee, Appl. Mater. Today 29 (2022) 101579.

[26] S. Burse, R. Kulkarni, R. Mandavkar, M.A. Habib, S. Lin, Y.-U. Chung, J.-H. Jeong, J. Lee, Nanomaterials 12 (2022) 3283.

[27] J. Fan, Z. Peng, M. Chen, W. Yang, H. Zou, S. Chen, Dalton Trans. 52 (2023) 6782–6790.

[28] S. Li, G. Zhang, X. Tu, J. Li, ChemElectroChem 5 (2018) 701–707.

[29] M.A. Habib, S. Burse, S. Lin, R. Mandavkar, M.H. Joni, J.H. Jeong, S.S. Lee, J. Lee, Small 20 (2024) 2307533 (n.d.).

[30] J. Chastain, R.C. King Jr, Perkin-Elmer, Corporation 40 (1992) 221.

[31] R. Tian, S. Zhao, J. Li, Z. Chen, W. Peng, Y. He, L. Zhang, S. Yan, L. Wu, R. Ahuja, H. Gou, J. Mater. Chem. A 9 (2021) 6469–6475.

[32] N. Chen, S. Che, H. Liu, G. Li, N. Ta, F. Jiang Chen, B. Jiang, N. Wu, Z. Li, W. Yu, F. Yang, Y. Li, J. Colloid Interface Sci. 638 (2023) 582–594.

[33] B. Bao, J. Liu, H. Xu, B. Liu, K. Zhang, Z. Jin, RSC Adv. 7 (2017) 8589–8597.

[34] S. Gupta, N. Patel, A. Miotello, D.C. Kothari, J. Power Sources 279 (2015) 620–625.

[35] Y. Wang, J. Wang, T. Xie, Q. Zhu, D. Zeng, R. Li, X. Zhang, S. Liu, Appl. Surf. Sci. 485 (2019) 506–512.

[36] J. Cen, P.K. Shen, Y. Zeng, J. Colloid Interface Sci. 610 (2022) 213–220.

[37] M. Bi, Y. Zhang, X. Jiang, J. Sun, X. Wang, J. Zhu, Y. Fu, Adv. Funct. Mater. 34 (2024) 2309330 (n.d.).

[38] Z. Pan, Z. Tang, D. Sun, Y. Zhan, Electrochim. Acta 436 (2022) 141393.

[39] H.S. Park, J. Yang, M.K. Cho, Y. Lee, S. Cho, S.D. Yim, B.S. Kim, J.H. Jang, H.K. Song, Nano Energy 55 (2019) 49–58.

[40] Y. Yang, Q.N. Yang, Y. Bin Yang, P.F. Guo, W.X. Feng, Y. Jia, K. Wang, W.T. Wang, Z.H. He, Z.T. Liu, ACS Catal. 13 (2023) 2771–2779.

[41] J.O.M. Bockris, T. Otagawa, J. Phys. Chem. 87 (1983) 2960–2971.

[42] I. Pathak, A. Muthurasu, D. Acharya, K. Chhetri, B. Dahal, Y.R. Rosyara, T. Kim, T. H. Ko, H.Y. Kim, J. Mater. Chem. A 12 (2024) 17544–17556.

[43] X. Gu, M. Yu, S. Chen, X. Mu, Z. Xu, W. Shao, J. Zhu, C. Chen, S. Liu, S. Mu, Nano Energy 102 (2022) 107656.

[44] X. Wang, H. Yao, C. Zhang, C. Li, K. Tong, M. Gu, Z. Cao, M. Huang, H. Jiang, Adv. Funct. Mater. 33 (2023) 1–12.

[45] R. Khan, M.T. Mehran, M.M. Baig, B. Sarfraz, S.R. Naqvi, M.B. Muhammad, M.Z. Khan, A.H. Khoja, Fuel 285 (2021) 119174.

[46] S. Li, W. Luo, Q. Gao, W. Shen, Y. Jiang, R. He, W. Su, M. Li, Appl. Surf. Sci. 637 (2023) 157940.

[47] D. Cao, X. Huang, H. Zhang, W. Liu, D. Cheng, Chem. Eng. J. 456 (2023) 141148.

[48] S. Loomba, M.W. Khan, M. Haris, S.M. Mousavi, A. Zavabeti, K. Xu, A. Tadich, L. Thomsen, C.F. McConville, Y. Li, S. Walia, N. Mahmood, Small 19 (2023) 2207310.

[49] Y. Xu, C. Wang, Y. Huang, J. Fu, Nano Energy 80 (2021) 105545.

[50] M. Plevová, J. Hnát, K. Bouzek, J. Power Sources 507 (2021) 230072.

[51] Q. Xu, L. Liang, T. Nie, Y. She, L. Tao, L. Guo, J. Phys. Chem. C 127 (2023) 5308–5320.

[52] S. Li, E. Li, X. An, X. Hao, Z. Jiang, G. Guan, Nanoscale 13 (2021) 12788–12817.

[53] X. Li, G.Q. Han, Y.R. Liu, B. Dong, W.H. Hu, X. Shang, Y.M. Chai, C.G. Liu, ACS Appl. Mater. Interface 8 (2016) 20057–20066.

[54] W. Rong, Y. Chen, R. Dang, K. Huang, J. Xia, B. Zhang, J. Liu, H. Meng, Q. Cao, J. Wu, J. Alloys Compd. 971 (2024) 172786.

[55] J. Mohammed-Ibrahim, H. Moussab, Mater. Sci. Energ. Technol. 3 (2020) 780–807.

[56] W. Sun, A. Meng, L. Wang, G. Li, J. Cui, Y. Sun, Z. Li, J. Energy Chem. 94 (2024) 29–40.

[57] Q. Ma, H. Jin, F. Xia, H. Xu, J. Zhu, R. Qin, H. Bai, B. Shuai, W. Huang, D. Chen, Z. Li, J. Wu, J. Yu, S. Mu, J. Mater. Chem. A 9 (2021) 26852–26860.

[58] X. Sun, P. Yang, S. Wang, J. Hu, P. Chen, H. Xing, W. Zhu, Int. J. Hydrogen Energy 47 (2022) 28495–28504.

[59] Y. Sang, X. Cao, G. Ding, Z. Guo, Y. Xue, G. Li, R. Yu, CrstEngComm 24 (2022) 199–207.

[60] L. Gu, Y. Li, A.D. Chowdhury, Mater. Today Chem. 27 (2023) 101290.

[61] W. Ma, Z. Qiu, J. Li, L. Hu, Q. Li, X. Lv, J. Dang, J. Energy Chem. 85 (2023) 301–309.

[62] Z. Wang, H. Chen, J. Bao, Y. Song, X. She, G. Lv, J. Deng, H. Li, H. Xu, Appl. Surf. Sci. 607 (2023) 154803.

[63] D. Chen, H. Bai, J. Zhu, C. Wu, H. Zhao, D. Wu, J. Jiao, P. Ji, S. Mu, Adv. Energ. Mater. 13 (2023) 2300499.

[64] F. Zhang, X. Wang, W. Han, Y. Qian, L. Qiu, Y. He, L. Lei, X. Zhang, Adv. Funct. Mater. 33 (2023) 2212381.

[65] Y. Wang, Q. Ye, L. Lin, Y. Zhao, Y. Cheng, J. Colloid Interface Sci. 651 (2023) 1008–1019.

[66] S. Chen, Z. Zheng, F. Wang, H. Wan, G. Chen, N. Zhang, X. Liu, R. Ma, ACS Sustain. Chem. Eng. 10 (2022) 15889–15897.

[67] X. Zhang, Y. He, B. Zhu, X. Wan, S. Hua, H. Tang, Int. J. Hydrogen Energy 48 (2022) 4686–4693.

[68] Y. Xue, X. Bai, Y. Xu, Q. Yan, M. Zhu, K. Zhu, K. Ye, J. Yan, D. Cao, G. Wang, Compos. B Eng. 224 (2021) 109229.

[69] J. Jiang, R. Sun, X. Huang, W. Xu, S. Zhou, Y. Wei, S. Han, Y. Li, Compos. B Eng. 263 (2023) 110834.

[70] F. Tang, Y.W. Zhao, Y. Ge, Y.G. Sun, Y. Zhang, X.L. Yang, A.M. Cao, J.H. Qiu, X.J. Lin, J. Colloid Interface Sci. 628 (2022) 524–533.

[71] A. Kumar, S.K. Purkayastha, A.K. Guha, M.R. Das, S. Deka, ACS Catal. 13 (2023) 10615–10626.

[72] L. Tan, J. Yu, H. Wang, H. Gao, X. Liu, L. Wang, X. She, T. Zhan, Appl. Catal. B Environ. 303 (2022) 120915.

[73] Y.T. Zeng, M.Y. Xu, T. Wang, S.Y. Wu, J. Zhang, S.C. Mu, J. Yu, Electrochim. Acta 444 (2023) 142004.

[74] B. Zhang, W. Li, K. Zhang, J. Gao, Y. Cao, Y. Cheng, D. Chen, Q. Wu, L. Ding, J. Tu, X. Zhang, C. Sun, J. Mater. Sci. Technol. 177 (2024) 214–223.

[75] G. Li, F. Yang, S. Che, H. Liu, N. Chen, J. Qian, C. Yu, B. Jiang, M. Liu, Y. Li, J. Mater. Sci. Technol. 166 (2023) 58–66.

[76] X. Yang, H. Shen, X. Xiao, W. Yang, Z. Li, N. Yang, L. Zhang, J. Mater. Sci. Technol. 204 (2025) 18–28.

[77] Y. Wang, P. Yang, Y. Gong, D. Liu, S. Liu, W. Xiao, Z. Xiao, Z. Li, Z. Wu, L. Wang, Chem. Eng. J. 468 (2023) 143833.

[78] Y. Fan, X. Zhang, Y. Zhang, X. Xie, J. Ding, J. Cai, B. Li, H. Lv, L. Liu, M. Zhu, X. Zheng, Q. Cai, Y. Liu, S. Lu, J. Colloid Interface Sci. 604 (2021) 508–516.

[79] Y. Zhang, L. Chen, B. Yan, F. Zhang, Y. Shi, X. Guo, Chem. Eng. J. 451 (2023) 138497.